aerospace

MDPI

Article

A Novel Approach to Ripple Cancellation for Low-Speed Direct-Drive Servo in Aerospace Applications

Xin Zhang, Ziting Wang *, Chaoping Bai and Shuai Zhang

National Space Science Center, Chinese Academy of Sciences, Beijing 100190, China; xinzhang@nssc.ac.cn (X.Z.); baichaoping@126.com (C.B.); zhangshuai@nssc.ac.cn (S.Z.)
* Correspondence: wangziting@nssc.ac.ac

Abstract: Low-frequency harmonic interference is an important factor that affects the performance of low-speed direct-drive servo systems. In order to improve the low-speed smoothness of direct-drive servo, firstly, the causes of the first and second harmonics of electromagnetic torque and tooth harmonics are analyzed based on the mathematical model of PMSM (permanent magnet synchronous motor) and the principle of vector control. Accordingly, the CC-EUMA (Electrical angle Update and Mechanical angle Assignment algorithm for Center Current) and SL-DQPR (Double Quasi-Proportional Resonant control algorithm for Speed Loop) algorithm are proposed. Second, to confirm the algorithm's efficacy, the harmonic environment is simulated using Matlab/Simulink, and the built harmonic suppression module is simulated and analyzed. Then, a miniaturized, fully digital drive control system is built based on the architecture of the Zynq-7000 series chips. Finally, the proposed suppression algorithm is verified at the board level. According to the experimental results, the speed ripple decreases to roughly one-third of its initial value after the algorithm is included. This effectively delays the speed ripple's low-speed deterioration and provides a new idea for the low-speed control of the space direct-drive servo system.

Keywords: low-speed; direct-drive servo; low-frequency harmonic current; permanent magnet synchronous motors; Zynq

check for updates

Citation: Zhang, X.; Wang, Z.; Bai, C.; Zhang, S. A Novel Approach to Ripple Cancellation for Low-Speed Direct-Drive Servo in Aerospace Applications. *Aerospace* **2024**, *11*, 834. https://doi.org/10.3390/aerospace11100834

Academic Editor: Dimitri Mavris

Received: 26 August 2024
Revised: 27 September 2024
Accepted: 8 October 2024
Published: 10 October 2024

1. Introduction

Owing to the unique features of the space application environment, which set the space servo apart from comparable equipment on Earth, its design principles need to include small size, light weight, low power consumption, and high reliability. As a result, the control system was initially powered by a conventional reducer before progressively switching to the motor direct-driven load "near-zero transmission" [1,2]. Because there is no need for a speed reduction device or other extra connecting parts, the structure is simpler and more reliable. With the rapid development of rare earth materials, PMSM has a wide speed range, high power density, and no low-frequency vibration phenomenon [3]. PMSM with multi-pole logarithms and high torque density may also produce enormous torque in the absence of gearboxes. Therefore, permanent magnet synchronous motor low-speed direct-drive servo systems have been widely employed in aerospace applications.

Direct drive transmission minimizes external input noise from a mechanical construction standpoint and reduces the weight of the machine, but at the same time, it also presents two additional problems [4–6]: (1) Low-speed noise is accentuated. In direct-drive transmission, the motor speed is the load speed; therefore, the motor has to run at a lower speed to match the low-speed requirement. A low-rotational-speed PMSM might result in low-speed jerks or low-speed crawling of the motor due to noise such as the body's natural cogging effect distorting the magnetic field in the air gap. (2) Harmonic disturbances are increased. Low-speed operation of the motor reduces phase current frequency, attenuates the rotational inertia filtering effect, amplifies body noise and various harmonic disturbances, and has a major negative impact on the system's low-speed performance. Thus, improving the low-speed stability of the system has become a research hotspot in the field of direct-drive servo.

Academics both domestically and internationally have conducted a number of studies aimed at resolving the aforementioned issues, starting with enhancing the motor body structure and refining the motor control approach. Different strategies have been effective in reducing current harmonics and improving low-speed performance. Under the premise that the fundamental wave of the air-gap magnet density is not attenuated, ref. [7] solves the ideal parameters of the permanent magnet form to accomplish efficient suppression of harmonic interference. Although the magnetic density harmonics can be lessened using this method, manufacturing assembly tolerances and material defects still remain [8], making it impossible to completely eliminate the harmonic components. The authors of [9] improved repetitive controllers with FIR filters in the current loop to suppress periodic disturbances. For the repetitive controller to effectively suppress harmonics, the system sample frequency needs to be an integer multiple of the harmonic fundamental frequency. The authors of [10] propose the construction of a harmonic current extraction module using a rotary PI (Proportional Integral) controller with a digital low-pass filter. It is not possible to detect a harmonic ripple using this method due to phase winding asymmetry or device electrical error of null position. Additionally, the digital low-pass filter needed for low-speed, lightly loaded servo systems has very low realizability and a low cut-off frequency. In [11], the harmonic components in the stator current were eliminated by building an extended state observer using a linear adaptive neural network. It extracts the harmonic currents from the feedback signal, estimates the torque disturbances and derives the optimal harmonic compensation components of the stator current. The authors of [12] estimated the cogging torque displacement curve for the optimum ripple correction using the observed data of cogging torque fluctuation with rotor position and the output data of the torque observer. Despite the greater control provided by this kind of neural network and torque observer approach, it requires more parameter calibration, has high system complexity, and its compensatory impact is readily affected by the nonlinear characteristics of the PMSM.

Furthermore, the demands of various control techniques vary with respect to computing power, speed of execution, and applications, leading to a variety of controller platforms. The driver is designed using a DSP + FPGA control architecture, as described in [13]. FPGA is in charge of processing logic instructions and current loops at a higher working frequency, while DSP handles top-level algorithms with lower frequency needs. The computational speed and efficiency of parallelism are better when there are separate heterogeneous multi-core processors; nevertheless, the hardware circuit design and inter-processor connection become more complex as a result of this architecture. Xilinx introduced the Zynq-7000 family of chips fully programmable System on Chip (SoC). It integrates both a software-programmable ARM processor and a hardware-programmable FPGA in the same chip [14]. This significantly decreased the difficulty of developing high-performance motor control system designs and opened up new avenues for thought.

In this paper, a direct-drive servo system is built with PMSM as the controlled object, a current-speed double-closed-loop PI controller as the basic framework, and Zynq-7015 chip as the driving core. As the servo system exhibits low-pass characteristics, this paper will analyze three forms of low-frequency harmonics that are more significant in causing speed ripple. For the first harmonic ripple of electromagnetic torque, a CC-EUMA algorithm is proposed to accurately suppress the superimposed DC bias in the phase current; for the second harmonic and tooth harmonic ripples of electromagnetic torque, an SL-DQPR algorithm is proposed, which combines the advantages of a fast response speed, easy control, and wide range of applicability while enhancing the accuracy of the speed loop in tracking the specific harmonics. In order to verify the correctness of the two control algorithms, harmonics are simulated in Matlab/Simulink and the performance of the algorithms is tested by simulation. Finally, the drive controller and the host computer platform were also built to verify the effectiveness and feasibility of the algorithm through experiments.

2. Causes of Low-Frequency Harmonic Current

Vector control simplifies electromagnetic torque control to the independent control of the excitation current and torque current in the dq coordinate system by decoupling the multivariate, strongly coupled mathematical model of PMSM in the ABC coordinate system in reduced order through coordinate transformation [15,16]. In the following analysis process, to simplify the calculation, the motor electromagnetic saturation, magnetic chain harmonics and eddy current losses are ignored.

2.1. DC Bias of Phase Current

The current sensor sampling method and armature winding series connection precision resistance method are two frequently utilized motor phase current detection approaches [17]. Phase current flows through the detection circuit, operational amplifiers, and low-pass filter to the ADC (Analog-to-Digital Converter) circuit; because of technological flaws in the chip and component, the phase current will be superimposed on the DC bias. For example, the sampling resistor's resistance deviation and temperature drift, and the three current sensors' varying reference voltages at 0 A, offset the voltage of the operational amplifier and the deviation of the lowest valid bit of the ADC. In the ABC coordinate system, the PMSM current equation for phase current superimposed on DC bias can be expressed as follows:

$$\begin{cases} I_{A1} = I\cos(\omega_e t + \varphi) + I_1 \\ I_{B1} = I\cos\left(\omega_e t + \varphi - \frac{2\pi}{3}\right) + I_2 \\ I_{C1} = I\cos\left(\omega_e t + \varphi + \frac{2\pi}{3}\right) + I_3 \end{cases} \tag{1}$$

where

I_{A1}, I_{B1}, and I_{C1} are the phase A, B, and C currents under DC bias, respectively. I is the peak value of the stator fundamental current. ω_e is the electrical angular velocity. t is time. φ is the initial phase of the stator fundamental current. I_1, I_2, and I_3 represent the DC bias in the three-phase windings. After the phase currents are transformed by Clark and Park, the equations in the dq coordinate system are as follows:

$$\begin{cases} I_{d1} = I\cos\varphi + I_1^*\sin(\omega_e t + \gamma_1) \\ I_{q1} = I\sin\varphi + I_1^*\cos(\omega_e t + \gamma_1) \end{cases} \tag{2}$$

where

$$\begin{cases} I_1^* = \sqrt{a_1^2 + b_1^2} \\ a_1 = \frac{2}{3}I_1 - \frac{1}{3}I_2 - \frac{1}{3}I_3 \\ b_1 = \frac{\sqrt{3}}{3}I_2 - \frac{\sqrt{3}}{3}I_3 \end{cases} \tag{3}$$

The above two equations are written as follows:

I_{d1} and I_{q1} are the d- and q-axes' currents under the action of DC bias, respectively. I_1^* is the peak value of the first harmonic of the torque current. γ_1 is the electrical angular fluctuation of the first harmonic. a_1 and b_1 are the DC components of the DC bias in the α- and β-axes, respectively. The electromagnetic torque, taking into account the first harmonic of the q-axis in the vector control mode with $I_d = 0$, may be expressed as follows:

$$T_e = \frac{P}{\omega_m} = p\varphi_f I\sin\varphi + p\varphi_f I_1^*\cos(\omega_e t + \gamma_1) \tag{4}$$

where T_e is the electromagnetic torque, ω_m is the mechanical angular velocity, P is the electromagnetic power, p is the number of pole pairs, and φ_f is the permanent magnet magnetic chain. The preceding analysis indicates that the phase current DC bias in the dq coordinate system is the sum of the DC component and the first harmonic component, where the first harmonic component causes the electromagnetic torque's first harmonic ripple. This seriously affects the low-speed performance of the servo system.

2.2. Gain Error of Phase Current

Assuming there is no DC bias in phase currents, we analyze the impact of gain error on system stability. In practical engineering, there is no such thing as a motor with equal parameters in all phases and a completely ideal back-end circuit. The phase current will display gain error if the phase inductance is asymmetric, the current sensor output sensitivity is biased, the ADC chip has quantization error, or the three circuits' impedance is imbalanced as a result of different circuit wiring lengths. The gain error-affected PMSM current equation can be written in the ABC and dq coordinate systems, respectively, as follows:

$$\begin{cases} I_{A2} = (I + \Delta I_1)\cos(\omega_e t + \varphi) \\ I_{B2} = (I + \Delta I_2)\cos(\omega_e t + \varphi - \frac{2\pi}{3}) \\ I_{C2} = (I + \Delta I_3)\cos(\omega_e t + \varphi + \frac{2\pi}{3}) \end{cases} \tag{5}$$

$$\begin{cases} I_{d2} = I\cos\varphi + I_{d2\_b} + I_2^* \sin(2\omega_e t - \gamma_2) \\ I_{q2} = I\sin\varphi + I_{q2\_b} - I_2^* \cos(2\omega_e t + \gamma_2) \end{cases} \tag{6}$$

where

$$\begin{cases} I_{d2\_b} = \frac{1}{3}(\Delta I_1 + \Delta I_2 + \Delta I_3)\cos\varphi \\ I_{q2\_b} = \frac{1}{3}(\Delta I_1 + \Delta I_2 + \Delta I_3)\sin\varphi \\ I_2^* = \frac{1}{2}\sqrt{c_2^2 + (b_2 - a_2)^2} \end{cases} \tag{7}$$

$$\begin{cases} a_2 = \frac{1}{6}(4\Delta I_1 + \Delta I_2 + \Delta I_3)\cos\varphi + \frac{\sqrt{3}}{6}(\Delta I_3 - \Delta I_2)\sin\varphi \\ b_2 = \frac{1}{2}(\Delta I_2 + \Delta I_3)\cos\varphi + \frac{\sqrt{3}}{6}(\Delta I_2 - \Delta I_3)\sin\varphi \\ c_2 = \frac{\sqrt{3}}{3}(\Delta I_3 - \Delta I_2)\cos\varphi + \frac{1}{3}(\Delta I_2 + \Delta I_3 - 2\Delta I_1)\sin\varphi \end{cases} \tag{8}$$

For the four equations above, the following information applies:

I_{A2}, I_{B2}, I_{C2}, I_{d2} and I_{q2} are the A, B, and C phase currents and the d- and q-axes' currents, respectively, under the influence of the gain error. ΔI_1, ΔI_2 and ΔI_3 are the current gain errors of the three-phase windings, respectively. I_{d2_b} and I_{q2_b} are the dc components of the gain error in the d-axis and q-axis. I_2^* is the peak value of the second harmonic; γ_2 is the electrical angular fluctuation of the second harmonic. a_2, b_2, and c_2 are the coefficients of the $\cos^2 \omega_e t$, $\sin^2 \omega_e t$, and $\cos\omega_e t \sin\omega_e t$ components of the gain error generated in the d-axis, respectively.

The electromagnetic torque can be written as follows:

$$T_e = p\varphi_f(I\sin\varphi + I_{q2\_b}) - p\varphi_f I_2^* \cos(2\omega_e t + \gamma_2) \tag{9}$$

The second harmonic component of the phase currents will be superimposed by the q-axis currents when there is a gain error in the phase currents, as can be seen from the above equation. This will result in the second harmonic ripple of the electromagnetic torque and worsen the system's performance.

2.3. Tooth Harmonic

Because of the relative distance between the rotor permanent magnets and the stator cogging slot, when the motor rotates, tooth harmonics superimpose in the magnetic circuit, producing the cogging torque [18]. The frequency f of the PMSM tooth harmonics can be expressed as follows [19,20]:

$$f_{ink} = \frac{ink}{60} = \frac{ifk}{p} \tag{10}$$

where: i is the number of tooth harmonics; n is the motor speed; k is the number of stator teeth; f is the stator fundamental frequency; let k/p = M.

The number of harmonics has a negative relationship with amplitude, as per the Taylor expansion of the cosine function. When the number of harmonics reaches a certain point, the influence becomes insignificant and the amplitude approaches zero. In this paper, we consider only the effect of the first-order tooth harmonic f_{nk} on the cogging torque, i.e., the Mth harmonic of the phase current.

The electromagnetic torque is only dependent on the AC component I_q when using the vector control strategy for $I_d = 0$. Figure 1 displays the current-speed double closed-loop servo system when cogging torque is applied, where ω_m^* is the desired mechanical angular velocity, $M_C(s)$ is the perturbation torque due to the cogging effect, ω_C is the mechanical angular velocity due to $M_C(s)$, $\omega_m^* + \omega_C$ is the actual mechanical angular velocity, I_q^* and I_q are the desired and actual values of the current loop, T_e is the electromagnetic torque setting value, $G_S(s)$ and $G_C(s)$ are the speed loop PI and current loop PI equivalent transfer functions, J is the motor moment of inertia, and $K(s)$ is the first-order equivalent link of the speed feedback. The transfer function between ω_C and $M_C(s)$ is

$$\frac{\omega_C(s)}{M_C(s)} = \frac{1}{Js + p\varphi_f K(s) G_S(s) G_C(s)} \tag{11}$$

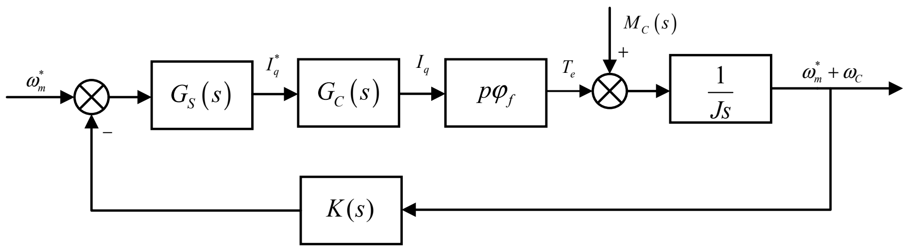

Figure 1. Double closed-loop servo system under the action of cogging torque.

In order to streamline the analysis, the speed loop, current loop controller, and speed feedback link in the given equation are referred to as proportional links K_S, K_C, and K, respectively. Based on the control system's frequency characteristics, the amplitude gain of ω_C may be represented as follows when $M_C(s)$ is pulsing at an angular velocity of ω_{nk}:

$$|\omega_C| = \frac{A}{\sqrt{\left(p\varphi_f K K_S K_C\right)^2 + (J\omega_{nk})^2}} \tag{12}$$

where A is the input torque ripple amplitude of the system. The angular velocity variation brought on by the cogging effect may be disregarded when PMSM is operating at a high speed, $\omega_m^* \to \infty$, $\omega_{nk} \to \infty$, and $|\omega_C| \to 0$. Large variations in angular velocity will result from the torque ripple when the PMSM runs at low speeds, $\omega_m^* \to 0$, $\omega_{nk} \to 0$, and $|\omega_C| = A/(p\varphi_f K K_S K_C)$. As the motor speed drops, it is evident that the cogging effect intensifies. For the speed smoothness to be equal to that of a high-speed servo, more ripple suppression is needed.

In summary, the cogging torque resulting from stator slotting causes additional pulsating torque when the PMSM rotates at low speeds. This torque causes Mth harmonic ripples, which lead to control deviations and noise in the system, without affecting the average effective torque of the motor.

3. Algorithms and Simulations for Suppressing Low-Frequency Harmonic Current

Given the many causes of harmonic creation, it is hard to achieve the best possible harmonic suppression efficiency when treating all three of the aforementioned harmonic current types together using a single compensatory strategy. This paper builds the control strategy from the sources of harmonic currents to weaken the different low-frequency harmonic components that account for a bigger share of the electromagnetic torque one by one, with the goal of optimizing the low-speed performance of the direct-drive servo system.

3.1. Principle of Low-Frequency Harmonic Current Suppression Algorithm

3.1.1. Electrical Angle Update and Mechanical Angle Assignment Algorithm for Center Current

The approach of solving phase currents using three equal and constant center currents is not effective due to the interference of sensor output bias and the electrical error of null location. This method raises the first harmonic content significantly and creates extra calculation bias. According to Equation (1), the DC bias superimposed on the cosine signal can be calculated by establishing a window with a width of 2π electrical angle and progressively sliding the integration of the phase currents within the window while the motor is rotating. The first harmonic ripple of electromagnetic torque can be reduced using this technique.

The position of the magnetic poles, the size of the permanent magnets, and the uniformity of the magnetization of the magnetic poles are not very satisfactory due to component manufacturing tolerances, and the asymmetric magnetic circuit will affect the stator's tooth count beneath the neighboring poles. The phase current waveforms of the pole pairs do not precisely coincide at any point during a motor rotation [21]; therefore, using continuous integral feedforward correction will result in a significant control divergence. But segmental integration based on the motor rotation's repeatability can yield a more accurate DC bias calculation, since the phase current waveform remains essentially unchanged when the rotor passes through the same place with every revolution. The segmented integration window beneath the magnetic pole pairs is therefore used by the CC-EUMA in place of the traditional electrical angle sliding integration window, as seen in Equation (13), where $\theta_e = \omega_e t$, θ_e is the rotor electrical angle. With this method, the DC bias of the stator winding may be accurately, efficiently, and quickly controlled. Furthermore, the CC-EUMA algorithm also configures three mean filters to smooth the center current at the integrating output while accounting for the potential impact of impulsive noise on the accuracy of the compensation.

$$\begin{cases} \int_0^{2\pi} [I\cos(\theta_e + \varphi) + I_1] d\theta_e = 2\pi I_1 \\ \int_0^{2\pi} [I\cos(\theta_e + \varphi - \dfrac{2\pi}{3}) + I_2] d\theta_e = 2\pi I_2 \\ \int_0^{2\pi} [I\cos(\theta_e + \varphi + \dfrac{2\pi}{3}) + I_3] d\theta_e = 2\pi I_3 \end{cases} \tag{13}$$

In particular, the CC-EUMA algorithm's execution may be split into the following three steps: (1) Segmental integrals within 2π electrical angles: According to the pole pair number p, the 2π mechanical angle for each motor rotation is divided into p electrical angle segments. The phase currents are then successively integrated to determine the center current of each phase current at the same location. (2) Integration result mean filtering: Three mean filter modules with window widths of m each are used to deposit the phase biases I_1, I_2, and I_3 into the same integration window for noise reduction. From there, the compensation value for the center current of each phase is determined, where $m \geq p$, and $m \in N^*$. (3) Center current cyclic assignment: A set of compensation values obtained in each cycle is temporarily stored in a register. To achieve the dynamic tracking of the center current, the DC bias at various points in each phase of the winding is updated cyclically with the mechanical angle since the initial dataset is valid.

As an illustration, Figure 2 depicts the use of the CC-EUMA algorithm for A-phase winding with a PMSM with a pole pair number of p of 2 and a mean-value filter with a window width m of 2, where the blue area represents the parameter that is calculated and updated in the current cycle.

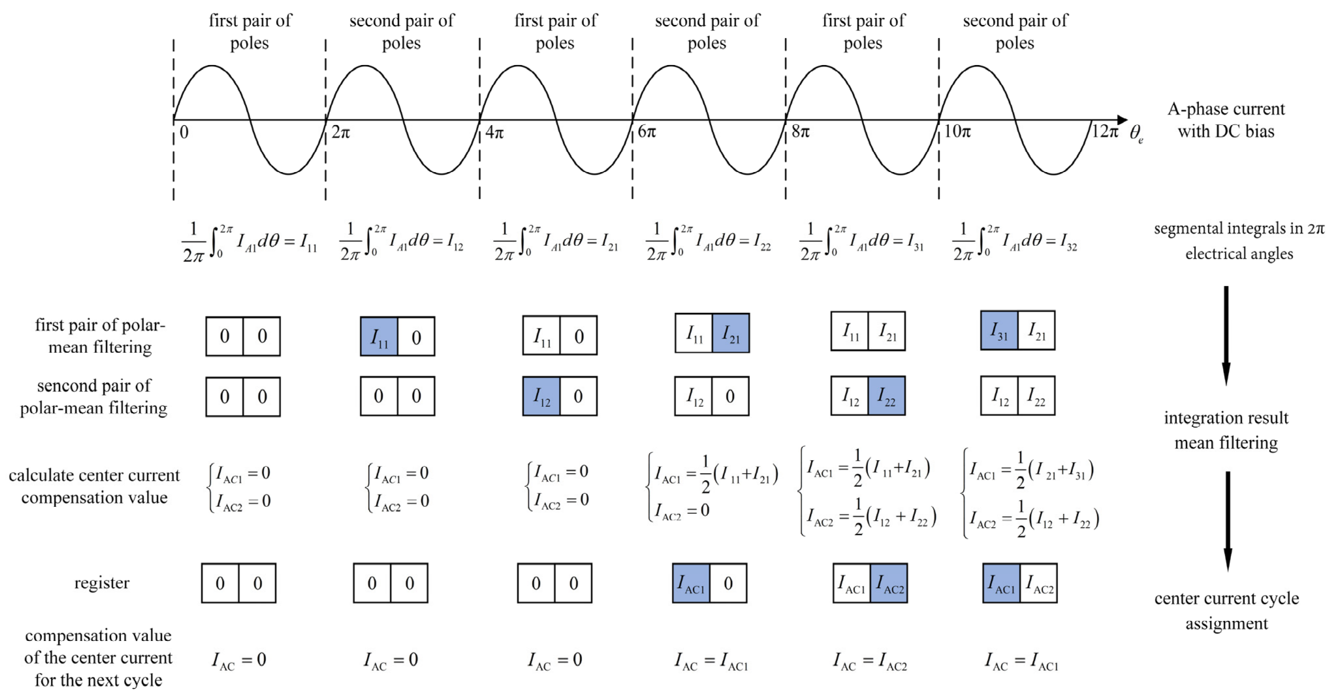

Figure 2. The algorithm of CC-EUMA.

3.1.2. Double Quasi-Proportional Resonant Control Algorithm for Speed Loop

According to the analysis in Section 2.2, the gain error of the phase current causes the second harmonic ripple of the electromagnetic torque. For integrals in the electrical angular range of 0–2π, Equation (5) yields zero, indicating that harmonic ripples brought on by phase current gain errors are not compensable by CC-EUMA. The PMSM phase inductance deviation directly affects the gain error of the phase current. An external inductor connected in series at the driving half-bridge's output can enhance the winding's symmetry, but the self-inductance and mutual inductance coefficients make it challenging to precisely calibrate the external inductor's value. The input disturbance amplitude, controller scaling factor, motor electromagnetic torque coefficient, rotational inertia, and stator teeth number are the pertinent variables that induce the second harmonic ripple of the electromagnetic torque, as can be observed from Equations (10) and (12). The four parameters, A, $p\varphi_f$, J, and k, are determined by the control system's structure and the decision's chosen motor characteristics. In addition, too-large controller parameters can easily lead to system oscillation and overshooting. To track periodic disturbances precisely or suppress them completely, the controller needs to incorporate an internal model of the periodic reference or periodic disturbances. The PR (Proportional Resonant) controller is an internal model of the cosine signal [22,23]. Equation (14) provides the PR controller's s-domain transfer function, where k_p is the proportionality coefficient, k_r is the resonance coefficient, and ω_0 is the resonant angular frequency.

Figure 3 displays the results of simulating and analyzing the amplitude–frequency characteristics of the PR controller when the settings are changed using the control variable approach, with the angular resonant frequency set to 2 Hz.

From the above figures, it can be seen that the high-gain band of the PR controller is narrow and the open-loop gain is infinite only at the resonant corner frequency. In order to reduce the system's sensitivity to the torque ripple frequency deviation, the QPR (Quasi-Proportional Resonant) controller is chosen to suppress the second and Mth harmonic disturbances. The transfer function of the QPR controller is as follows:

$$G_{\mathrm{QPR}}(s) = k_p + \frac{2k_r\omega_c s}{s^2 + 2\omega_c s + \omega_0^2} \tag{14}$$

where ω_c is the cut-off frequency. The purpose of ω_c is to increase the resonant bandwidth and reduce the system's susceptibility to the torque ripple's frequency variation. The amplitude–frequency characteristic curve of the QPR controller, produced by the simulation, is displayed in Figure 4, where $\omega_c = 0.05\omega_0$, using the same scaling and resonance coefficients as the PR controller.

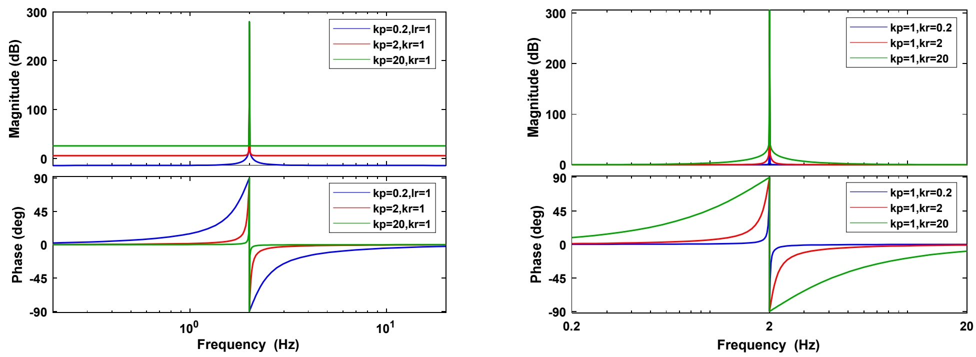

(**a**) (**b**)

Figure 3. Amplitude–frequency characteristics of the PR controller: (**a**) k_p is a variable constant, k_r is an invariant constant; (**b**) k_p is an invariable constant, and k_r is a variant constant.

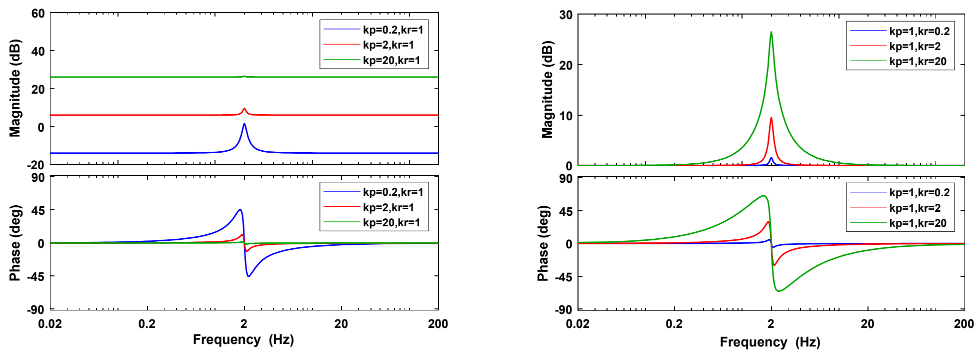

(**a**) (**b**)

Figure 4. Amplitude–frequency characteristics of the QPR controller. (**a**) k_p is a variable constant, k_r is an invariant constant; (**b**) k_p is an invariable constant, and k_r is a variant constant.

Equation (6) and vector control theory demonstrate that rotational speed superposition with harmonic ripple of the same frequency occurs when there are harmonic disturbances in the torque current. In the case of the speed loop, the single controlled parameter ω_m can be achieved independently for harmonic suppression by a single QPR controller, whereas the two controlled parameters I_d and I_q of the current loop require the synergistic cooperation of two QPR controllers in order to ensure that $I_d = 0$ and I_q are regulated correctly. Obviously, the speed loop single-group QPR controller has the benefit of having a strong anti-disturbance ability and more easily modifiable settings than the two-group QPR controller with the quadrature axis and direct axis of current loop. Because of this, this paper presents the SL-DQPR algorithm, an improved speed loop control strategy that reduces the impact of the second harmonic and the tooth harmonic on the accuracy of the speed control by connecting the QPR controllers with resonant frequencies $2f$ and f_{nk} in parallel with the speed loop PI controller.

The system's Baud diagram is displayed in Figure 5 before and after the speed loop's parallel QPR controllers, with the values of ω_0 and ω_c for each controller being set to 500 Hz, 1500 Hz, 5 Hz, and 15 Hz. As shown in the figure, the QPR controller not only keeps the control system tracking characteristics at the resonance point, but it also simultaneously enhances the system's bandwidth and anti-frequency fluctuation characteristics, making it a valuable tool for engineering applications.

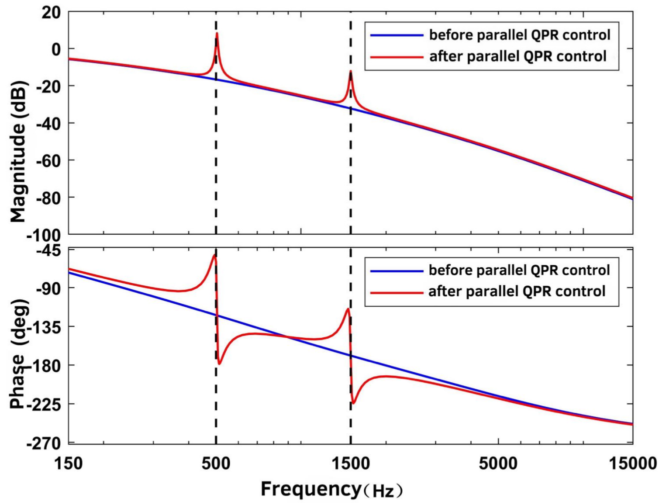

Figure 5. Baud diagram of the system before and after parallel QPR control in a speed loop.

3.2. Simulation of Low-Frequency Harmonic Current Suppression Algorithm

The control model is constructed using Matlab/Simulink (Version 2020b) and the harmonic environment is simulated based on the suggested CC-EUMA and SL-DQPR. Analyzing the variations in speed ripple and harmonic content before and after the algorithm's addition shows how effective the algorithms are. The air-gap magnetic field distortions caused by nonlinearities such as phase current DC bias, gain error, and the motor cogging effect are not included in the Simulink simulation because it is based on an ideal PMSM model. To assess the effectiveness of the suggested control strategy, the first, second, and Mth harmonics of the phase currents are simulated in the simulation by adjusting the phase current DC bias, changing the stator inductance scaling factor, and superimposing the higher harmonic currents, respectively. The chosen motor's phase inductance for simulation is 2 mH and its pole pair count is 1. When the motor is operating at 5 rad/s speed without any load, the phase current fundamental frequency is around 0.796 Hz.

3.2.1. Simulation of CC-EUMA

The DC bias module seen in Figure 6 is designed to superimpose a DC bias into the phase currents through the addition unit Add_IX, thus producing the first harmonic ripple of the torque current. Figure 7 depicts the CC-EUMA algorithm module, which is made up of several first-order delay units, multipliers, and discriminators. The * in Figure 7 represents multiplication. Equation (16) illustrates the approximate way of calculating the integral calculus using the trapezoidal method, where n is the present moment and $t_\theta(n)$, $u_I(n)$, and $y_I(n)$ are the electrical angle, phase current, and integral output at the present moment, respectively.

$$y_I(n) = y_I(n-1) + \frac{1}{2}[u_I(n) + u_I(n-1)] \times [t_\theta(n) - t_\theta(n-1)] \tag{15}$$

The first harmonic component of the speed signal is increased by the DC bias of the phase currents, as shown in Figures 8 and 9. By employing CC-EUMA, the speed ripple is decreased from 0.234% to 0.012% and the first harmonic content of the speed is decreased from 0.217558% to 0.00025%.

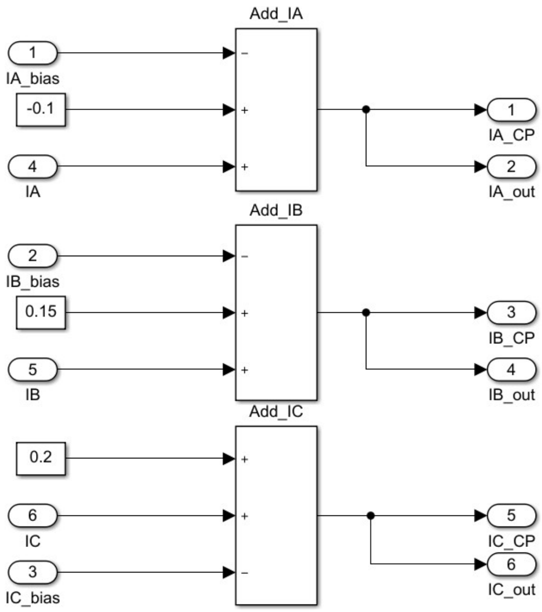

Figure 6. DC bias module used to simulate torque current's first harmonic.

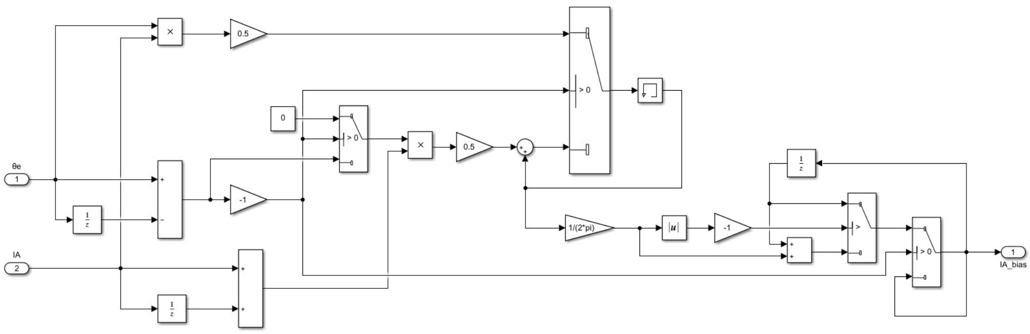

Figure 7. CC-EUMA algorithm module.

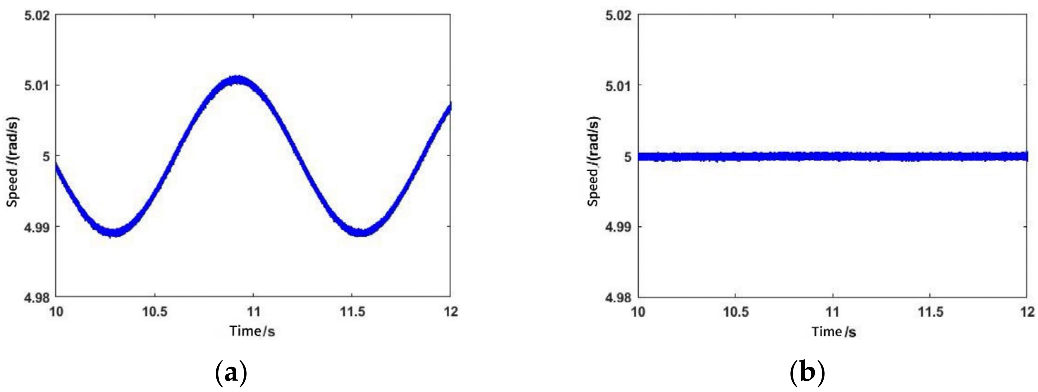

Figure 8. Simulation results of speed before and after adding CC-EUMA: (**a**) before adding CC-EUMA; (**b**) after adding CC-EUMA.

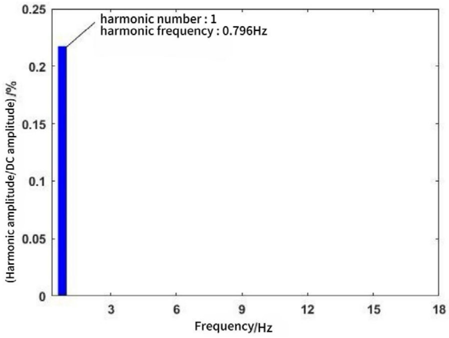

(**a**)

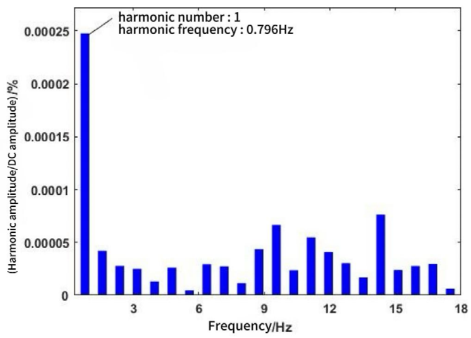

(**b**)

Figure 9. Simulation results of speed FFT before and after adding CC-EUMA: (**a**) before adding CC-EUMA; (**b**) after adding CC-EUMA.

3.2.2. Simulation of SL-DQPR

The motor model under Simulink is modified in two ways to confirm that the SL-DQPR control technique can successfully reduce the electromagnetic torque ripple brought on by the phase current gain error and the body cogging effect. One way is to build an asymmetric motor model. Figure 10a shows the PMSM after the inductors have been modified. The motor's A and B phase windings are both linked in series with 0.1 mH inductors and the C phase's inductance value is left intact. Another method involves simulating the stator notch effect. The torque current and excitation current are injected with an interference signal at the same frequency as the tooth harmonic, 11.144 Hz, which is the 15th harmonic of the phase current, as seen in Figure 10b.

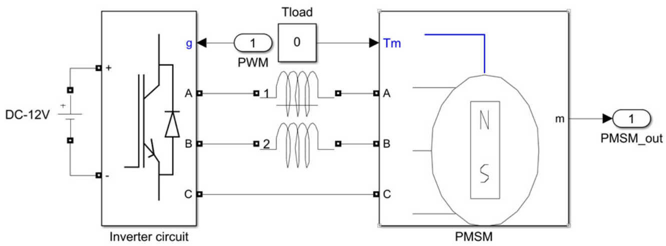

(**a**)

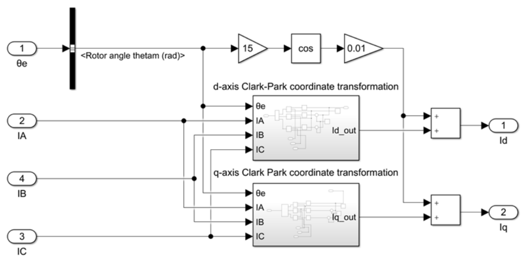

(**b**)

Figure 10. Module structure for torque current simulation of the second and tooth harmonics: (**a**) analog second harmonic; (**b**) analog tooth harmonic.

In the simulation model, the parameters of the QPR controller for suppressing the second and tooth harmonics of the phase current are set as follows: (1) ω_0 = 1.592 Hz, ω_c = 0.2 Hz, k_p = 80, k_r = 2.2; (2) ω_0 = 11.94 Hz, ω_c = 0.7 Hz, k_p = 40, k_r = 2. The SL-DQPR module, which primarily comprises the speed loop PI controller, the phase current second harmonic suppression module QPR_2f, and the tooth harmonic suppression module QPR_fnk, is depicted in Figure 11 with dual QPRs concurrently linked in parallel to the speed loop. In Figure 11, * represents the set value of the parameter.

As can be shown from Figure 12, prior to the addition of SL-DQPR, the speed ripple is 0.082%, the speed distortion is clearly visible, and the harmonic components make up a significant percentage of the speed. The fluctuation is significantly decreased and the speed ripple is decreased to 0.021%, or around one-quarter of the initial value, with the addition of SL-DQPR. The speed FFT comparison is displayed in Figure 13, where the use of the SL-DQPR algorithm reduces the motor speed's second harmonic content from 0.0541% to 0.0078% and its Mth harmonic content from 0.0165% to 0.0025%. In conclusion, it is evident that SL-DQPR effectively suppresses both Mth order and secondary torque ripples.

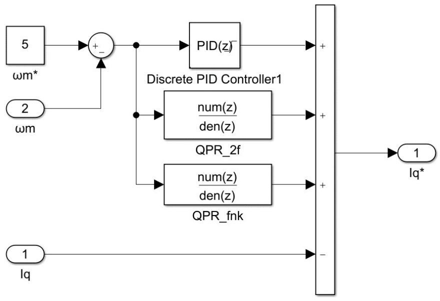

Figure 11. SL-DQPR algorithm module.

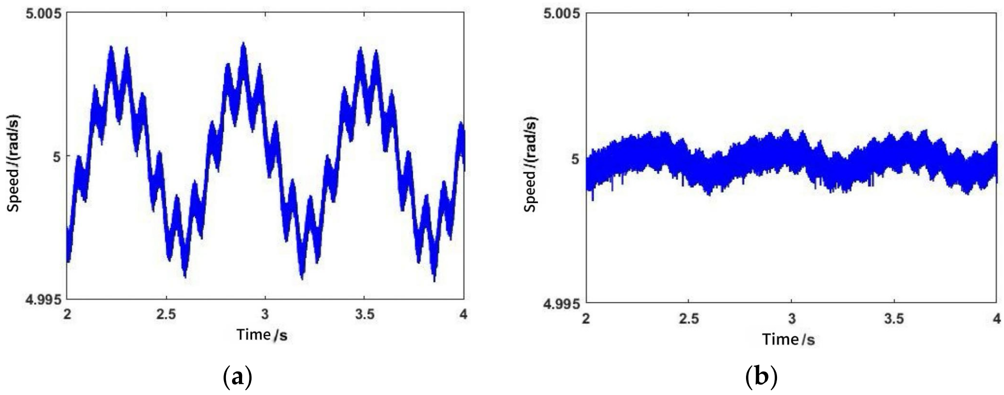

Figure 12. Simulation results of speed before and after adding SL-DQPR: (**a**) before adding SL-DQPR; (**b**) after adding SL-DQPR.

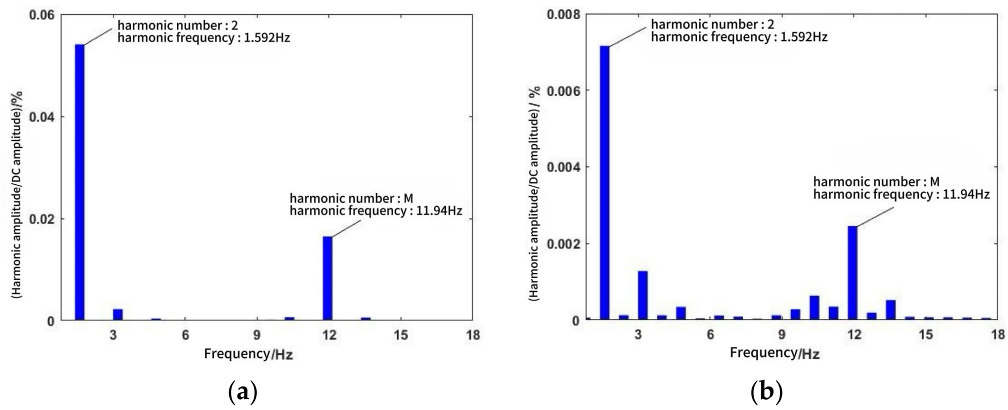

Figure 13. Simulation results of speed FFT before and after adding SL-DQPR: (**a**) before adding SL-DQPR; (**b**) after adding SL-DQPR.

4. PMSM Direct-Drive Servo System Design

As seen in Figure 14, the PMSM direct-drive servo system is composed of three components: the servo mechanism, the drive controller, and the master computer. Through the serial link, the master computer issues target orders to the drive controller, which uses the gathered parameters to solve the six PWM signals with dead time and pull the servo mechanism. Once the FPGA side receives the first valid data packet, the motor data packets stored in the block random access memory are transmitted over the serial bus to the host computer platform for data processing and display monitoring.

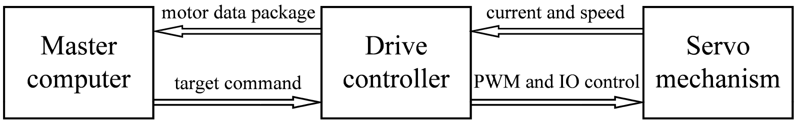

Figure 14. Servo system architecture.

4.1. Design of the Drive Controller

Arithmetic and timing logic are closely linked to servo control, and the controller's floating-point capabilities undergo heavy strain resulting from the hardware implementation of harmonic suppression methods. Considering the needs of an intelligent, compact, digital space mission, the drive controller chose the Zynq-7015 peripheral circuits based on the power supply, speed-current monitoring, optocoupler isolation, and motor drive modules working together. Figure 15 shows this framework.

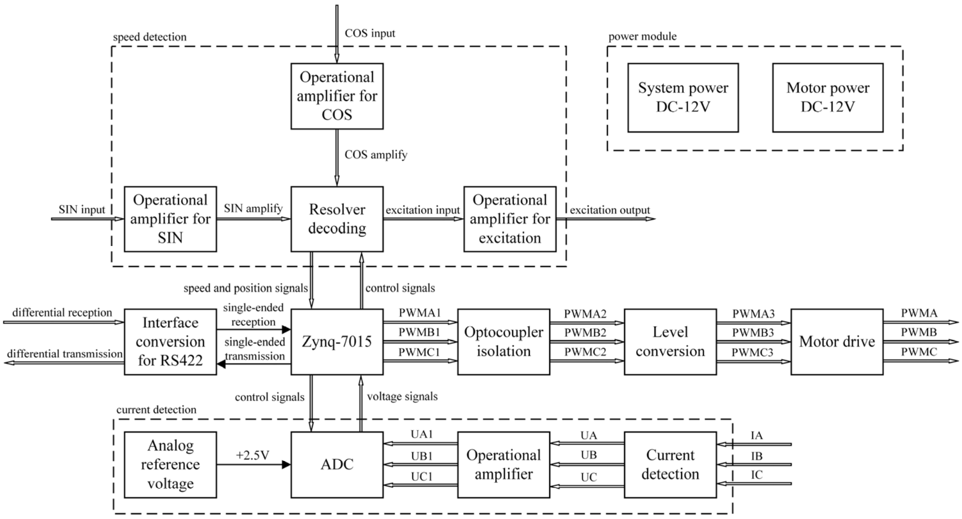

Figure 15. Structure of the drive controller.

The overall design framework of the controller is based on the dual PI control of current speed. The massive magnetoresistive current sensor is used in the inner current loop, and its sensitivity to weak currents may be efficiently increased by the four huge magnetoresistors forming a Whisden bridge structure. The RDC (Resolver to Digital Converter) is used for the speed loop to analyze the rotor speed information by using the Type II tracking closed-loop principle. As the central component of the controller, the Zynq-7015 processes sensor detection data in high-speed parallel and outputs the PWM of each phase that rotates the motor, enabling full closed-loop control.

4.2. Design of the Software Control System

The system software is accomplished through the synergy between the PL and the PS in order to maximize the performance of the Zynq-7015 multicore Processor (cf. Figure 16). In Figure 16, * represents the set value of the parameter. The PL is in charge of controlling the motor's drive. Its main functional modules include system timing control, SVPWM data solving, and sample data forwarding and storage. The PS is responsible for the implementation of the top-level algorithm. The phase currents in the ABC coordinate system are processed by the CC-EUMA, coordinate transformation, and SL-DQPR modules to determine the voltages in the $\alpha\beta$ coordinate system. These values are then sent to the PL side for data transmission using the AXI4 bus's burst transfer mechanism.

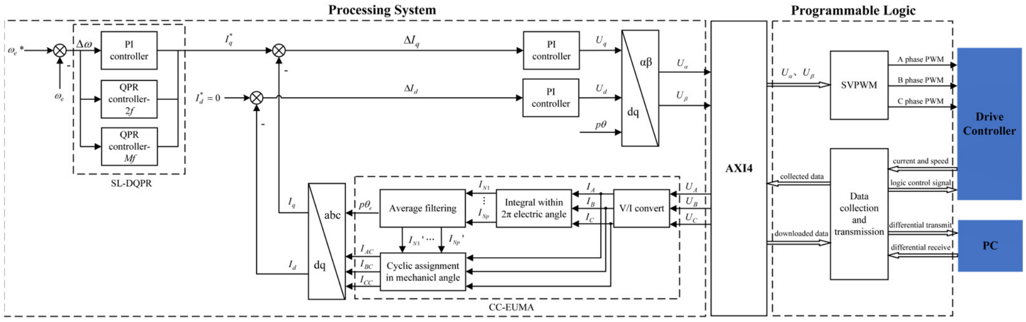

Figure 16. Software architecture of PMSM low-speed direct-drive servo system.

To achieve fully digital servo control and improve the detecting equipment, an interactive master computer system for measurement and control was constructed using the Labview platform. Six event structures make up the state machine that constitutes the master computer's fundamental building block. It allows for real-time system status information to be displayed and facilitates online parameter changes (cf. Figure 17).

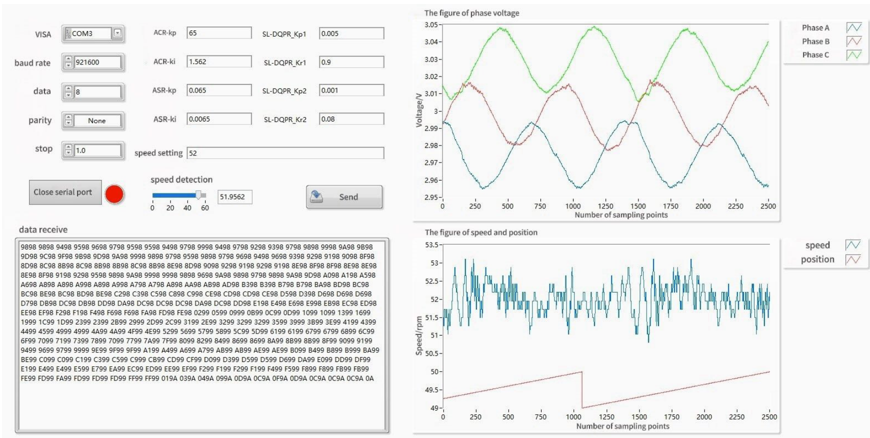

Figure 17. Operational interface of the master computer system.

5. Experimental Results and Discussion of the Servo System

5.1. Experimental Test Platform for the System

The power supply, drive controller, permanent magnet synchronous motor, resolver, oscilloscope, and upper computer make up the majority of the servo system experimental test platform, as seen in Figure 18. Figure 19 shows the self-built driver controller's internal hardware circuit.

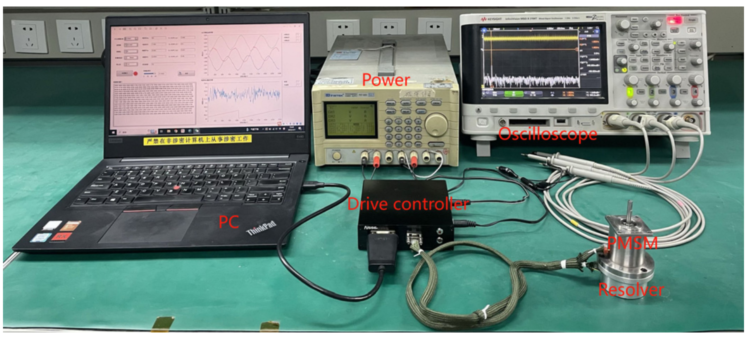

Figure 18. Experimental platform for the servo system.

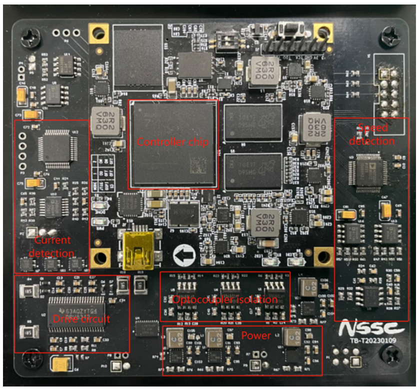

Figure 19. Internal hardware components of the drive controller.

Figure 20 illustrates the system's timing control flow. The system's control frequency, which is 5 kHz, is the same as the PWM frequency. Because PWM level jumps might lead to sampling mistakes, the motor driven signal's sample beginning point is chosen to be in the middle of the PWM. The average value of three successive samples is chosen by the system as reliable data for this sampling. ADC and RDC have successive sampling frequencies of 166 kHz and 136 kHz, respectively. At the halfway point of the control cycle, the drive pulse's duty cycle is updated, and the synchronization is activated to accept control orders from the host computer. The SVPWM computation for the subsequent location must be finished within 100 µs of the control cycle's zero moment in order to guarantee that each PWM cycle generates a legitimate driving signal.

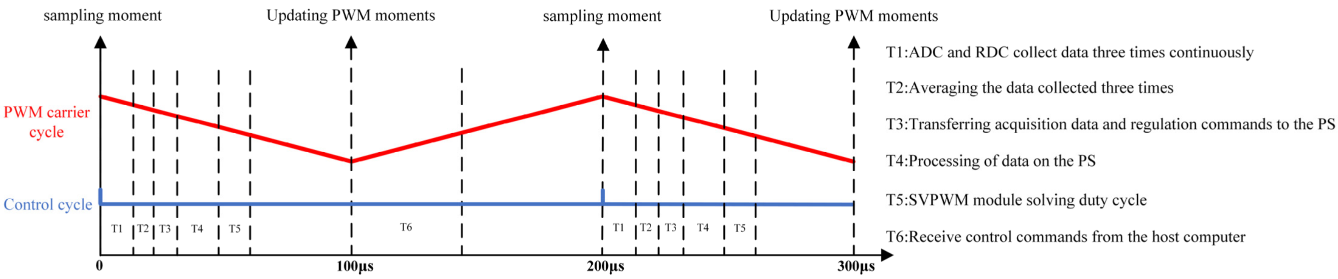

Figure 20. Timing control flow of the system.

5.2. Experimental Results and Discussion of Harmonic Suppression Algorithms

The motor with fewer pole pairs was chosen for the experiment due to the light load application, which ensures that the motor's output mechanical power is used in its entirety. The parameters of the PMSM are rated voltage U_r = 12 V, number of pole pairs p = 2, number of stator teeth k = 30.

This part tests five low-speed modes with fixed speeds of 50 rpm, 40 rpm, 30 rpm, 20 rpm, and 10 rpm with the motor unloaded in order to confirm the improvement of the two algorithms on the smooth functioning of the motor at low speeds. During the test, the executable code of the CC-EUMA algorithm is first injected into the controller and then the SL-DQPR algorithm is added on the basis that the DC bias of the phase current has been weakened, thereby highlighting its effect of suppressing the motor torque ripple.

5.2.1. Experimental Validation of CC-EUMA

Figues 21a–25a show the speeds of the servo system before and after adding CC-EUMA. Prior to the algorithm being included, there were clear periodic oscillations in the speed waveform. The waveform tended to be smoother and the speed variations were greatly reduced once the algorithm was included. Table 1 displays the speed variance, tracking error, and speed ripple of the motor at five different speeds derived from the processing of the experimental data before and after CC-EUMA was added to the system.

The test results in the table show that CC-EUMA enhances the low-speed stability of the system and has a strong ripple suppression impact at varied speeds.

Table 1. Parameter comparison before and after adding CC-EUMA at different speeds.

Parameter	CC-EUMA	50 rpm	40 rpm	30 rpm	20 rpm	10 rpm
Speed variance	Before adding	1.314	0.914	0.684	0.327	0.105
	After adding	0.336	0.261	0.247	0.157	0.074
Tracking error	Before adding	1.892%	1.999%	2.235%	2.241%	2.553%
	After adding	0.928%	1.045%	1.326%	1.612%	2.209%
Speed ripple	Before adding	5.000%	5.352%	6.766%	7.865%	10.112%
	After adding	2.975%	3.429%	4.546%	5.682%	6.818%

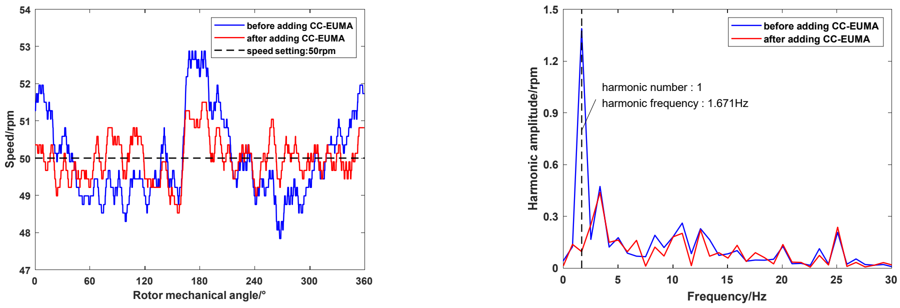

(**a**) (**b**)

Figure 21. Speed and speed FFT before and after adding CC-EUMA at 50 rpm: (**a**) speed; (**b**) speed FFT.

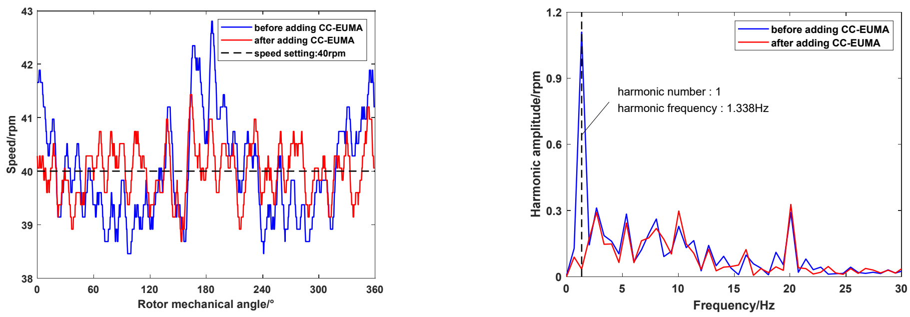

(**a**) (**b**)

Figure 22. Speed and speed FFT before and after adding CC-EUMA at 40 rpm: (**a**) speed; (**b**) speed FFT.

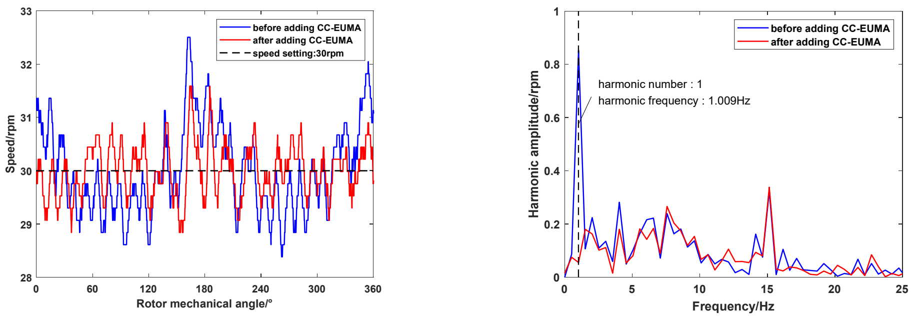

(**a**) (**b**)

Figure 23. Speed and speed FFT before and after adding CC-EUMA at 30 rpm: (**a**) speed; (**b**) speed FFT.

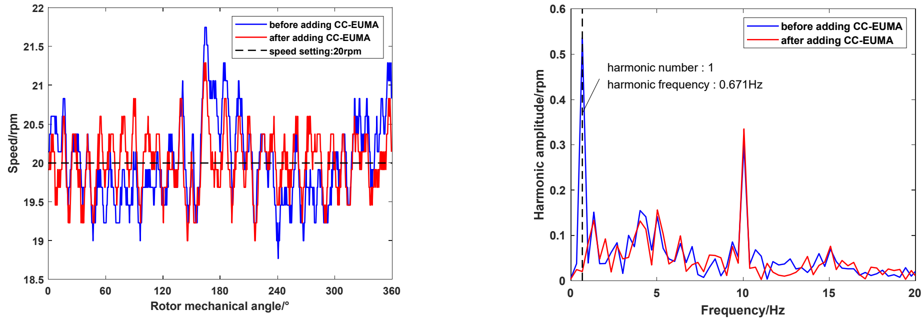

(**a**) (**b**)

Figure 24. Speed and speed FFT before and after adding CC-EUMA at 20 rpm: (**a**) speed; (**b**) speed FFT.

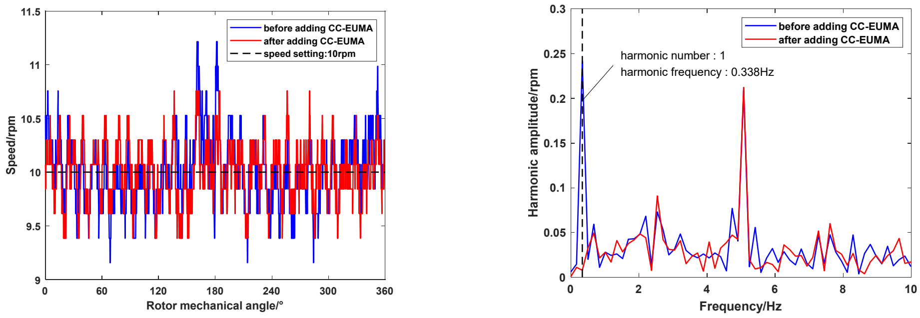

(**a**) (**b**)

Figure 25. Speed and speed FFT before and after adding CC-EUMA at 10 rpm: (**a**) speed; (**b**) speed FFT.

The FFT transforms of the speed signals before and after adding the CC-EUMA are shown in Figures 21b–25b, and the signal frequencies marked by the dashed lines are the fundamental frequencies of the phase currents. Table 2 displays the amplitude changes in the first harmonic overlaid on the speed signal before and after CC-EUMA was added to the control system in each of the five operating modes. It is evident from the reduction in the first harmonic amplitude to around 1/14, 1/32, 1/15, 1/28, and 1/30 of the original one that the CC-EUMA proposed in this paper is capable of successfully reducing the DC bias of the phase currents of the motors with asymmetric magnetic circuits.

Table 2. Comparison of the first harmonic amplitude before and after adding CC-EUMA at different speeds.

Speed	50 rpm	40 rpm	30 rpm	20 rpm	10 rpm
Before adding CC-EUMA	1.388 rpm	1.101 rpm	0.852 rpm	0.536 rpm	0.242 rpm
After adding CC-EUMA	0.096 rpm	0.034 rpm	0.056 rpm	0.019 rpm	0.008 rpm

5.2.2. Experimental Validation of SL-DQPR

The rotational speeds before and after the addition of SL-DQPR at various rotational speeds are compared in Figrues 26a–30a, based on the addition of CC-EUMA. Following the addition of the algorithm, the speed data are computationally processed, resulting in the comparative results shown in Table 3. The speed ripple is successfully reduced and the system's low-speed stability is greatly enhanced following the parallel connection of double QPR controllers in the speed loop. At 50 and 40 rpm, the speed ripple is less than 2% and the tracking error is less than 0.7%; at 30 and 20 rpm, the speed ripple is less than 3% and the tracking error is less than 1%; and at 10 rpm, the torque ripple is less than 3.5% and the tracking error is less than 1.5%.

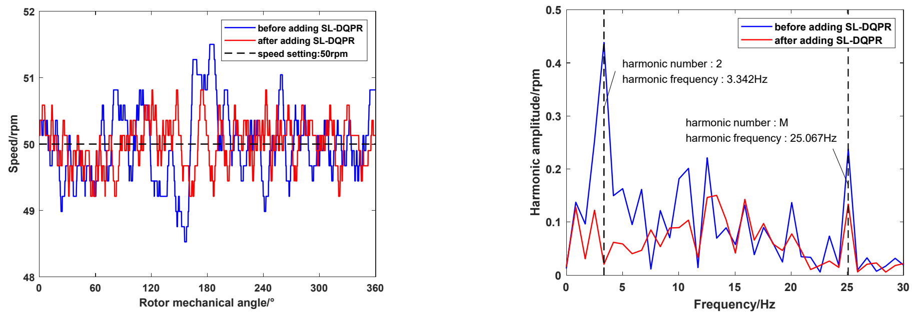

(**a**) (**b**)

Figure 26. Speed and speed FFT before and after adding SL-DQPR at 50 rpm: (**a**) speed; (**b**) speed FFT.

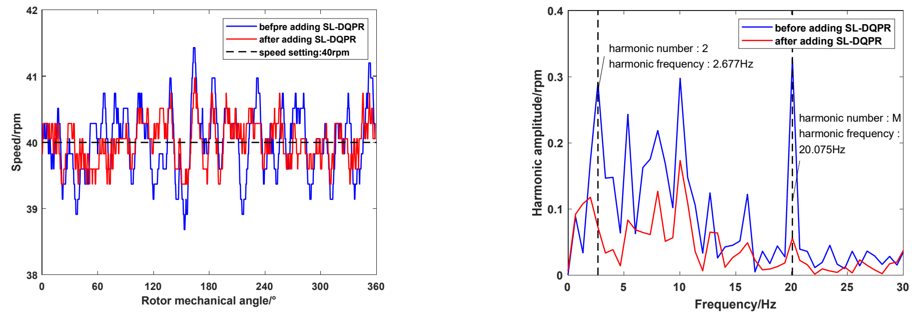

(**a**) (**b**)

Figure 27. Speed and speed FFT before and after adding SL-DQPR at 40 rpm: (**a**) speed; (**b**) speed FFT.

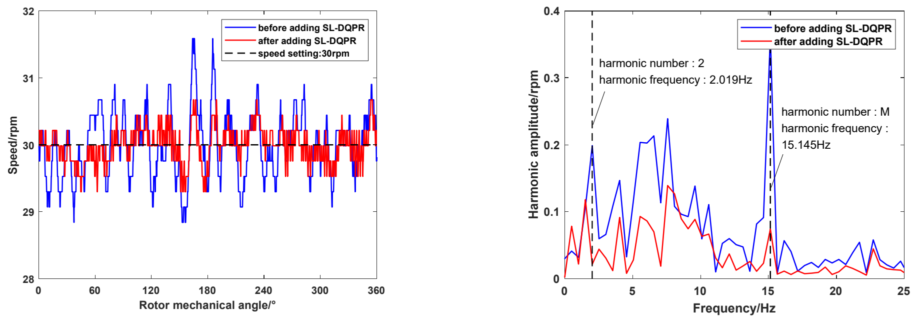

(**a**) (**b**)

Figure 28. Speed and speed FFT before and after adding SL-DQPR at 30 rpm: (**a**) speed; (**b**) speed FFT.

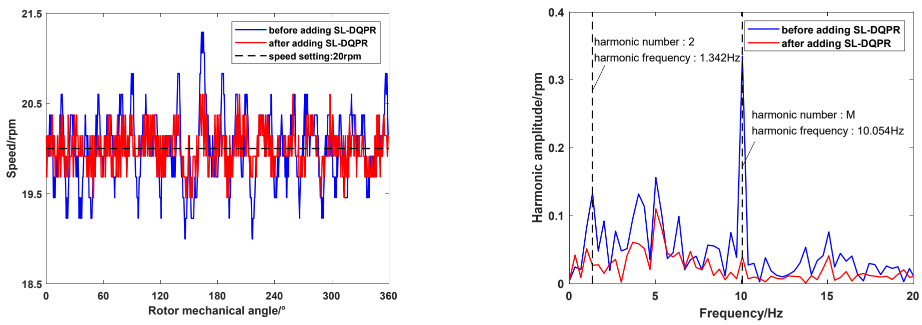

(**a**) (**b**)

Figure 29. Speed and speed FFT before and after adding SL-DQPR at 20 rpm: (**a**) speed; (**b**) speed FFT.

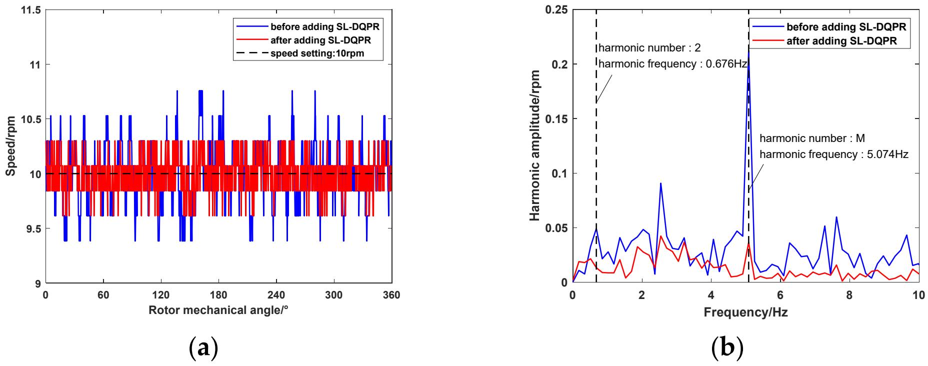

Figure 30. Speed and speed FFT before and after adding SL-DQPR at 10 rpm: (**a**) speed; (**b**) speed FFT.

Table 3. Parameter comparison before and after adding SL-DQPR at different speeds.

Parameter	SL-DQPR	50 rpm	40 rpm	30 rpm	20 rpm	10 rpm
Speed variance	Before adding after adding	0.336 0.1272	0.261 0.106	0.247 0.309	0.157 0.052	0.074 0.028
Tracking error	Before adding after adding	0.928% 0.591%	1.045% 0.671%	1.326% 0.666%	1.612% 0.826%	2.209% 1.429%
Speed ripple	Before adding after adding	2.975% 1.602%	3.429% 1.994%	4.546% 2.290%	5.682% 2.857%	6.818% 3.448%

To facilitate a more intuitive observation of the suppression of each harmonic by SL-DQPR, a spectrally analyzed speed signal is used, with dashed lines designating the second and Mth harmonics of the phase currents in Figures 26b–30b. Table 4 illustrates how the SL-DQPR harmonic compensation effect efficiently attenuates the second and Mth harmonics. Specifically, at a speed of 50 rpm, the second harmonic amplitude is lowered by approximately 20 times, while at a speed of 20 rpm, the M harmonic amplitude is reduced by approximately 10 times. In addition, it can be seen from the speed spectrogram that the second harmonic and Mth harmonic are weakened by the action of the cutoff frequency and resonance coefficients in the QPR controllers, and certain low-frequency noises near the resonance frequency are suppressed synchronously. This experimental result confirms that SL-DQPR can effectively and simultaneously suppress the Mth order torque ripples and the secondary torque ripples of permanent magnet synchronous motors.

Table 4. Comparison of second harmonic amplitude before and after adding SL-DQPR at different rotational speeds.

Parameter	SL-DQPR	50 rpm	40 rpm	30 rpm	20 rpm	10 rpm
Second harmonic ripple	Before adding After adding	0.438 rpm 0.021 rpm	0.291 rpm 0.073 rpm	0.199 rpm 0.022 rpm	0.133 rpm 0.027 rpm	0.049 rpm 0.013 rpm
Mth harmonic ripple	Before adding After adding	0.237 rpm 0.134 rpm	0.327 rpm 0.056 rpm	0.364 rpm 0.074 rpm	0.335 rpm 0.039 rpm	0.212 rpm 0.037 rpm

The body noise of the permanent magnet synchronous motor will be more audible when the direct-drive servo is operating at a low speed. Furthermore, different low-frequency disturbances will be enhanced due to the phase current fundamental frequency reduction, but the low-pass characteristics of the servo system will not change. These phenomena cause the system's speed fluctuations to become more noticeable. The speed ripple and speed ripple suppression ratio are compared in Figure 31 and Table 5, respectively, before and after CC-EUMA and SL-DQPR are added at five different speeds. The speed ripple suppression ratio η_r is used to measure the degree of control algorithm's suppression of harmonic ripple, which can be expressed as follows:

$$\eta_r = \frac{\eta_f - \eta_l}{\eta_f} \tag{16}$$

where η_f and η_l are the speed ripples before and after adding the algorithm, respectively.

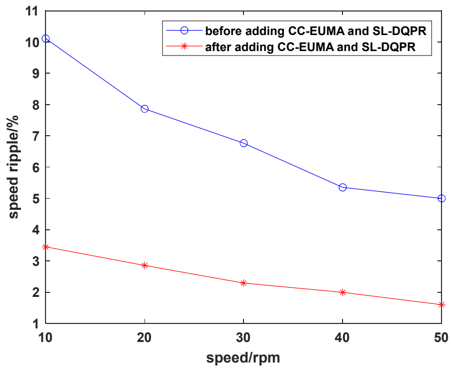

Figure 31. The speed ripples of adding CC-EUMA and SL-DQPR at the same time.

Table 5. Speed ripple suppression ratio after adding CC-EUMA and SL-DQPR at different speeds.

Speed	50 rpm	40 rpm	30 rpm	20 rpm	10 rpm
Speed ripple Suppression ratio	67.960%	62.743%	66.154%	63.675%	65.902%

The blue curve in Figure 31 illustrates how the speed ripple's increasing rate tends to increase quickly when the speed decreases. The ripple at each test point is effectively suppressed and the low-speed deterioration of the speed ripple is postponed after using the two control strategies suggested in this paper, as indicated by the red curve in Figure 31. It can also be seen from Table 5 that both algorithms still contribute significantly to the reduction of speed ripples even at 10 rpm.

6. Conclusions

Within the framework of low-speed servo system applications in space, the paper analyzes the generating mechanisms of the first, second, and Mth harmonics of electromagnetic torque. Based on this analysis, the CC-EUMA and SL-DQPR algorithms are presented. Following theoretical research, simulation verification, and extensive harmonic suppression experiments lead to the following conclusions:

- Output bias of current detecting elements, asymmetry of stator windings, and the cogging effect are three common phenomena in low-speed direct-drive servo systems, and even slotless motors are not immune to first and second harmonic ripples.
- The three different kinds of low-frequency harmonics are more effectively suppressed by CC-EUMA and SL-DQPR. When the motor speed is 10 rpm, after adding the two algorithms, the speed ripple suppression ratio of the system is better than 66%, i.e., the speed ripple is reduced to about one-third of the original.
- With the Zynq-7015 serving as the control core, the design maximizes the benefits of co-developing software and hardware. Our attempt provides a reference for the development of miniaturized and intelligent space low-speed scanning mechanism, which has good engineering application value.

This paper takes the suppression of low-frequency harmonic currents as the starting point to design the control algorithm, which improves the low-speed performance of the direct-drive servo system to some extent. The increasing needs of space missions mean that further investigation is still required, and we recommend the following steps:

- Conduct dynamic performance tests to analyze the dynamic performance of the system. Tests that may be performed include step response tests, motor load step change tests, and speed control response times tests. Keep track of how long it takes the motor drive to return the system to normal functioning and how it reacts to unforeseen changes in the operating environment.
- Try to adopt an AI chip combined with servo control to realize the digitalization and intelligence of servo control. With the rapid development of high-performance AI chips, the use of AI chips to realize the adaptive adjustment of optimal parameters will be considered in the future to improve the immunity of the system.
- Conduct environmental reliability experiments. Mechanical, thermal vacuum, and EMC experiments, etc., can be conducted based on the instrument's operating environment to completely confirm the system's dependability.

Author Contributions: Conceptualization, X.Z. and Z.W.; methodology, Z.W.; software, Z.W.; validation, Z.W., C.B. and S.Z.; formal analysis, X.Z.; investigation, S.Z.; resources, X.Z.; data curation, Z.W. and C.B.; writing—original draft preparation, Z.W.; writing—review and editing, X.Z. All authors have read and agreed to the published version of the manuscript.

Funding: This research received no external funding.

Data Availability Statement: The data are contained in the article.

Conflicts of Interest: The authors declare no conflicts of interest.

References

1. Zhai, S.X.; Wang, C.S.; Tan, L. Driving and controlling of high accuracy scanning servo-system in space. *Opt. Precis. Eng.* **2016**, *24*, 1104–1111. [CrossRef]
2. Pazdera, I.; Huták, P.; Procházka, P. Speed Estimator for Low Speed PMSM Aerospace Application. In Proceedings of the 12th International Conference on Mechatronics, Brno, Czech Republic, 6–8 September 2017; pp. 452–457.
3. Fang, S.H.; Liu, H.; Wang, H.T.; Yang, H.; Lin, H.Y. High Power Density PMSM With Lightweight Structure and High-Performance Soft Magnetic Alloy Core. *IEEE Trans. Appl. Supercond.* **2019**, *29*, 0602805. [CrossRef]
4. Niu, S.X.; Ho, S.L.; Fu, W.N. A Novel Direct-Drive Dual-Structure Permanent Magnet Machine. *IEEE Trans. Magn.* **2010**, *46*, 2036–2039. [CrossRef]
5. Balakrishnan, J.; Govindaraju, C. Multi-Phase Permanent Magnet Generator with Halbach Array for Direct Driven Wind Turbine: A Hybrid Technique. *Energy Sources Part A Recovery Util. Environ. Eff.* **2022**, *44*, 5699–5717. [CrossRef]
6. Xia, X.Q.; Zhang, B.; Li, X.T. High Precision Low-Speed Control for Permanent Magnet Synchronous Motor. *Sensors* **2020**, *20*, 1526. [CrossRef] [PubMed]
7. Liu, C.; Xu, Y.; Zou, J.; Yu, G.; Zhuo, L. Permanent Magnet Shape Optimization Method for PMSM Air Gap Flux Density Harmonics Reduction. *CES Trans. Electr. Mach. Syst.* **2021**, *5*, 284–290. [CrossRef]
8. Cernigoj, A.; Gasparin, L.; Fiser, R. Native and Additional Cogging Torque Components of PM Synchronous Motors—Evaluation and Reduction. *Automatika* **2010**, *51*, 157–165. [CrossRef]
9. Jianbo, C. Method of Suppressing the Periodic Disturbance of Motor Based on Repetitive Controller. *Electr. Drive* **2010**, *40*, 48–51.
10. Yong, L.; Shuai, Z.; Ren, L.I.U.; Jun, Y.A.O. Torque Ripple Suppression of Permanent Magnet Synchronous Motor by the Harmonic Injection. *Proc. Chin. Soc. Electr. Eng.* **2011**, *31*, 119–127.
11. Qu, J.Z.; Zhang, C.N.; Jatskevich, J.; Zhang, S. Deadbeat Harmonic Current Control of Permanent Magnet Synchronous Machine Drives for Torque Ripple Reduction. *IEEE J. Emerg. Sel. Top. Power Electron.* **2022**, *10*, 3357–3370. [CrossRef]
12. Mora, A.; Orellana, A.; Juliet, J.; Cárdenas, R. Model Predictive Torque Control for Torque Ripple Compensation in Variable-Speed PMSMs. *IEEE Trans. Ind. Electron.* **2016**, *63*, 4584–4592. [CrossRef]
13. Gao, Y. Research on Control Technology of Direct Drive Servo System Using Permanent Magnet Synchronous Motor under Low Speed Rang for Aerospace Application. Master's Thesis, Nanjing University of Aeronautics and Astronautics, Nanjing, China, 2020.
14. Ramagond, S.; Yellampalli, S.; Kanagasabapathi, C. A Review and Analysis of Communication Logic between PL and PS in ZYNQ AP SoC. In Proceedings of the International Conference on Smart Technologies for Smart Nation (SmartTechCon), Bengaluru, India, 17–19 August 2017; pp. 946–951.
15. Cai, J.; Deng, Z.Q. Initial Rotor Position Estimation and Sensorless Control of SRM Based on Coordinate Transformation. *IEEE Trans. Instrum. Meas.* **2015**, *64*, 1004–1018. [CrossRef]

16. Fu, X.H.; He, H.; Chen, W.; Zou, J.B.; He, X.K. Decoupled Vector Control of PMSM Based on Uncertainty and Disturbance Estimator. In Proceedings of the International Conference on Electrical Machines (ICEM), Gothenburg, Sweden, 23–26 August 2020; pp. 1099–1104.
17. Xiao, Y. Research on Servo Motor Resolver and Sin/Cos Encoder Zero Point Calibration System. Master's Thesis, Huazhong University of Science and Technology, Wuhan, China, 2012.
18. Arand, S.J.; Ardebili, M. Cogging torque reduction in axial-flux permanent magnet wind generators with yokeless and segmented armature by radially segmented and peripherally shifted magnet pieces. *Renew. Energy* **2016**, *99*, 95–106. [CrossRef]
19. Wang, C.Y.; Xia, J.K.; Sun, Y.B. *Modern Control Technology for Electric Machines*; China Machine Press: Beijing, China, 2014.
20. Güemes, J.A.; Iraolagoitia, A.M.; Fernández, P.; Donsión, M.P. Comparative study of PMSM with integer-slot and fractional-slot windings. In Proceedings of the XIX International Conference on Electrical Machines-ICEM 2010, Rome, Italy, 6–8 September 2010; pp. 1–6.
21. Zhang, W.H.; Li, J.H.; Xu, L. Experimental analysis of torque fluctuation in permanent magnet DC torque motors. *Micromotors* **2004**, *37*, 64–66. [CrossRef]
22. Xia, C.L.; Ji, B.N.; Yan, Y. Smooth Speed Control for Low-Speed High-Torque Permanent-Magnet Synchronous Motor Using Proportional-Integral-Resonant Controller. *IEEE Trans. Ind. Electron.* **2015**, *62*, 2123–2134. [CrossRef]
23. Francis, B.A.; Wonham, W.M. Internal Model Principle of Control-Theory. *Automatica* **1976**, *12*, 457–465. [CrossRef]